TECHNICAL ARTICLE

An elementary method to generate asymmetric profiles and some applications in X-ray diffraction analysis

Abraham Gutierrez, [1] and Manfred Wiessner [2, a)]
[1] *Institute of Analysis and Number Theory, TUGraz , 8010 Graz, Austria*
[2] *Anton Paar GmbH , Anton-Paar-Str. 20, 8054 Graz, Austria*

(Received 29 December 2023; accepted 11 November 2024)

We present a versatile method to generate asymmetric profiles and use it to create Gaussian-like, Cauchy-like, and Pseudo-Voigt-like profiles in terms of elementary functions. Furthermore, this method guarantees that the position and magnitude of the global maximum are independent of the asymmetry parameter, which substantially facilitates the convergence of an optimizer when fitting the peaks to real data. This investigation shows that the method developed here exhibits favorable practical properties and is particularly well suited for various applications where asymmetric peak profiles are observed. For example, in X-ray diffraction (XRD) measurements, the use of asymmetric profiles is essential for obtaining accurate outcomes. This is because diffractometers can introduce asymmetry into the diffraction peaks due to factors such as axial divergence in the beam path. By taking this asymmetry into account during the modeling process, the resulting data obtained can be corrected for instrumental effects. The results of the study show that the evaluation of XRD using nearly defect-free LaB_6 allows a precise characterization of the peak broadening caused by the diffractometer itself. Additional size-strain effects of ZnO are determined by considering the asymmetric peak profile of the diffractometer.
© *The Author(s), 2024. Published by Cambridge University Press on behalf of International Centre for Diffraction Data.*
[doi:10.1017/S0885715624000587]

Keywords: asymmetric profiles, asymmetric profile construction, elementary functions, XRD measurements, instrumental effects correction

I. INTRODUCTION

X-ray diffraction (XRD) is a widely used technique used in material characterization, particularly for polycrystalline materials. The microstructure of such materials strongly affects their mechanical properties, among others, and can be determined using XRD (Mittemeijer and Scardi, 2013). One important aspect of XRD analysis is the determination of the line profile shapes of individual diffraction peaks. For example, the peaks' positions, together with Bragg's equation (Bragg and Bragg, 1913), provide information about the materials contained in the sample, while peak areas are used to determine phase quantities using the Rietveld method (Rietveld, 1967, 1969). It is worth mentioning that the relative intensity ratio (RIR) method can alternatively be used to determine the quantitative phase content, where the peak areas are referenced relative to the corundum. For further details, please refer to the literature (e.g., Hubbard et al., 1976; Davis, 1989, 1992).

Other properties of the profiles, such as peak broadening and asymmetry, also provide valuable information: the peak broadening is related to the lattice defect density (Alexander, 1954; Balzar and Ledbetter, 1994) and the asymmetry is connected to the instrumental broadening (Cheary et al., 2004).

In XRD , different methods are available for representing asymmetric peaks. The "Fundamental Parameter Model" by Cheary and Coelho (1998), is commonly used to characterize the broadening effect caused by the slit system, which is then convoluted with the peak broadening effects of the specimen. This convolution is often implemented in software packages such as TOPAS (Coelho, 2018) or GSASII (Toby and Von Dreele, 2013; Denney et al., 2022). Alternatively, phenomenological presentations, such as the use of split-peaks, are also available in software packages like HighScore (Degen et al., 2014) for representing asymmetric peaks. In this work, we propose a novel elementary method for generating representative asymmetric profiles that capture the line profile shapes of individual diffraction peaks. The method described herein can be applied to elementary profiles. Symmetric elementary profiles are extended for the asymmetric case. It is noteworthy that when the asymmetry parameters used in this work are set to 0, the asymmetric profiles transform into their corresponding symmetric versions.

The presented method offers an alternative approach to fitting measurements, resulting in precise determinations of peak positions and peak broadening caused by the instrument itself and caused by lattice defects within the phases. The main advantage of the method presented in this paper is the clear relationship between the parameters that define the profiles and their properties; in particular, the construction method keeps the position and magnitude of the global maximum, independent of the asymmetry parameters (The independence

[a)] Author to whom correspondence should be addressed. Electronic mail: wiessner_manfred@yahoo.de

https://doi.org/10.1017/S0885715624000587 Published online by Cambridge University Press

of the position and magnitude of the global maximum with respect to the asymmetry parameter is something that, to our best knowledge, is not found in the mathematical or physics literature concerning elementary asymmetric profiles e.g. (Cheary et al., 2004; Gupta et al., 2004; Huang and Chen, 2007; Korepanov and Sedlovets, 2018). There are, however, non-elementary profiles that fulfill the property (e.g. Kern, 1998) but are hard to work with in practice.), see Propositions 2, and 3. The low correlation among the profile's parameters is particularly useful when fitting XRD's data with many peaks, because it substantially facilitates the convergence of the optimizer. Furthermore, the profiles that are showcased in this paper [see Eqs (5), (6) and (8)] are constructed with elementary functions. This eases the numeric calculations that are needed to extract additional mathematical properties of the profiles (e.g., area, FWHM, and convolution – see subsections III.C, III.D, and III.E), from which, physical properties of the examined material can be retrieved.

The paper is organi zed as follows: Section II , Proposition 2 describes the general method for the construction of profiles with convenient properties on the global maxima. In Section III, we apply Proposition 2 to construct asymmetric Gaussian, Cauchy, and Pseudo-Voigt profiles. In Section IV, we fit real XRD data with the Pseudo-Voigt-like profile, analyze the quality of this fit with various metrics, and compare it with the fit of the symmetric Pseudo-Voigt profile. Finally, in Section V , we discuss the results and provide a summary of the paper.

II. GENERAL METHOD TO CONSTRUCT PROFILES

In this section, we present a general method to construct new functions with desirable properties on their global maxima and their magnitudes. We begin by introducing some definitions and a proposition that will be used in the subsequent analysis.

Definition 1.

"Iff" stands for "if and only if," which is used to denote a necessary and sufficient condition. That is, the statement "P iff Q" means "P is true if Q is true, and P is true only if Q is true".

Definition 2.

The empty set is denoted as $\emptyset$. In particular, if a set A has at least one element, we denote this as $A \neq \emptyset$.

Definition 3.

A function f taking an input from a set A and returning an output in a set B will be denoted as $f{:}A \to B$, and it is also said to be a function from A to B . In particular, a function f with an input and output in the real numbers R will be denoted as $f{:}R \to R$, and it is said to be a function from R to R .

The notation in Definition 3 means that f is a function that maps elements from the set of real numbers (input) to the set of real numbers (the output).

Definition 4.

Let $f{:}R \to R$ be differentiable. A critical point x_0 of f is a point such that $f'(x_0) = 0$. Furthermore, the (possibly empty) set of critical points of f will be denoted as $C(f)$.

In mathematics, a critical point of a function is a point where the derivative is zero. Critical points are important in analyzing the behavior of functions because they can indicate locations of local maxima, local minima, or saddle points.

Definition 5.

Let $f{:}D \to R$ be a function. A global maximum x_m of f is an element of D such that $f(x_m) \geq f(x)$ for any $x \in D$. We denote the (possibly empty) set of global maxima of f as $M(f)$. Notice there might be more than one global maximum. Also, notice that every global maximum has the same magnitude; this magnitude will be referred as $max(f)$.

Definition 6.

Let $f{:}D \to R$ be a function. A point x_m in D is called the absolute maximum of f iff x_m is the only global maximum of f.

Definition 7.

Let $f{:}D \to R$ be a function and A be a set of real values. The preimage of A under f is the (possibly empty) set $\{r \in D{:}f(r) \in A\}$ and will be denoted by $f^{-1}(A)$. Notice that the preimage always exists, which is not the case with the inverse function.

For Definition 7, the term "preimage" should be clarified: The preimage of a function is the set of all input values that, when passed through the function, produce a specific output or range of outputs. It can be thought of as working backward from the output to find all possible inputs that could have resulted in that output.

The following elementary proposition will be used later in this section and it is written for the sake of completeness. It states that if you have two smooth (differentiable) functions, f and w, that take real numbers as inputs and outputs, then you can determine the critical points of the combined function.

Proposition 1

Let f and w be differentiable functions from R to R , then

$$C(f \circ w) = w^{-1}(C(f)) \cup C(w) \qquad (.)$$

Proof.

Applying the chain rule, we get the following expression $(f \circ w)'(x) = f'(w(x))w'(x)$, which is zero iff $w(x) \in C(f)$ or $x \in C(w)$. In other words, the expression is zero iff. $x \in w^{-1}(C(f)) \cup C(w)$ ■

Proposition 1 can be described in words as follows: Given f and w, two differentiable functions, then the preimage under w of the critical points of f, i.e. $w^{-1}(C(f))$ union the set of critical points of w, i.e. $C(w)$ is equal to the set of critical points of f composed with w, i.e. $C(f^{\circ} w)$.

The next proposition is the main point in this section and can be informally described as a set of conditions to construct new functions with "good" behaviors on the global maxima and their magnitudes. The importance of this proposition

https://doi.org/10.1017/S0885715624000587 Published online by Cambridge University Press

will be clear when we apply it (see Proposition 3) to prove the independence of the global maxima and their magnitudes from the asymmetry parameter a of the showcased profiles [see Eqs (5), (6), and (8)]. As stated in Definition 4, the set of critical points of f will be denoted as $C(f)$, and as defined in Definition 5, the set of global maxima of f will be denoted as M(f).

Proposition 2.

(Profile Construction Method). *Let $f:R \to R$ be a function with $M(f) \neq \emptyset$ (with at least one global maximum) and let w: $R \to R$ be a function such that $w^{-1}(M(f)) \neq \emptyset$ (the preimage of w contains at least one critical point of f), then $f^{\circ} w:R \to R$ satisfies:*

- $max(f \circ w) = \max(f)$
- $M(f \circ w) = w^{-1}(M(f))$

In *particular, if f and w are differentiable and $C(w) = \emptyset$ (i.e. w has no critical points) and there is a $\mu \in R^{+}$ such that $M(f) = C(f) = \{\mu\}$ (i.e. μ is the only critical point and the absolute maximum of f) and the preimage $w^{-1}(\{\mu\}) = \{\mu\}$ (where $\{\mu\}$ is a set with the single element μ), then we have that $C(f \circ w) = M(f \circ w) = \{\mu\}$, i.e. μ is the only critical point and the absolute maximum of $f \circ w$.*

Proof.

Let f and w be functions from R to R in the first part of the proposition. Now, let $x \in R$, then by definition we have that $f \circ w(x) = f(w(x)) \leq maxf$ and equality is valid iff $x \in w^{-1}(M(f))$, which proves that $M(f \circ w) \supseteq w^{-1}(M(f))$. By assumption, $M(f) \neq \emptyset$ and $w^{-1}(M(f)) \neq \emptyset$, therefore there is $x_0 \in R$ such that $f \circ w(x_0) = maxf$ which proves that $max(f \circ w) = maxf$ and that $M(f^{\circ} w) \subseteq w^{-1}(M(f))$. The last two contentions prove that $M(f \circ w) = w^{-1}(M(f))$. This concludes the proof of the first part of the proposition.

Let f and w be as in the second part of the proposition. Then, by Proposition 1, we get that $C(f \circ w) = w^{-1}(C(f)) \cup C(w) = \{\mu\}$, since $w^{-1}(C(f)) = \{\mu\}$ and $C(w) = \emptyset$, by assumption. Furthermore, by the first part of the current proposition, we have that $M(f \circ w) = w^{-1}(M(f)) = w^{-1}(\{\mu\}) = \{\mu\}$ and this implies that of μ is the absolute maximum of $f^{\circ} w$ because $M(f^{\circ} w)$ has a single element. This concludes the proof of the proposition.■

Proposition 2 allows us to construct new profiles from old ones by using "asymmetry functions". A detailed description of the method is given below.

1. Choose profile: We choose a function $f:R \to R$ with a point x_m that satisfies the following:

- f is differentiable;
- x_m is the only critical point of f ;
- x_m is the absolute maximum of f .

2. Choose asymmetry function: Let A be a non-empty set of R . We choose a function $w:R \times A \to R$, such that for any fixed choice of a in A , the function $w(\cdot, a):R \to R$ denoted as w_a , satisfies the following:

- w_a is differentiable;
- w_a has no critical points;
- The preimage of x_m (the global maximum of f) under w_a is the point x_m itself. Formally written, $w_a^{-1}(\{x_m\}) = \{x_m\}$.

3. New profile: For any fixed choice of $a \in A$, the new function $f^{\circ} w_a:R \to R$ satisfies the following properties:

- $f^{\circ} w_a$ is differentiable;
- x_m is the only critical point of $f^{\circ} w_a$;
- x_m is the absolute maximum of $f^{\circ} w_a$;

The magnitude of the absolute maximum of $f^{\circ} w_a$ is independent of the value a . More precisely, $f \circ w_a(x_m) = f(x_m)$;

The magnitude of the absolute maximum of $f \circ w_a$ is equal to the magnitude of the absolute maximum of f . Formally written, $max(f \circ w_a) = maxf$.

III. SHOWCASED PROFILES

In this section, we define the proposed asymmetric profiles [see Eqs (5), (6), and (8)] and study different properties of them with respect to the asymmetry parameter: position of the global maxima and magnitude (see subsection III.B), area (see subsection III.C), FWHM (see subsection III.D), and convolutions (see s ubsection III.E). The asymmetric Pseudo-Voigt-like profile is later used to fit XRD data (see subsection IV.B and IV.C).

A. Symmetric and asymmetric profiles

Let us briefly recall the symmetric Gaussian g, Cauchy c, and Pseudo-Voigt p (approximation of the Voigt profile) distributions :

$$g(x, \mu, \sigma) = \frac{1}{\sigma\sqrt{2\pi}} e^{-\frac{1}{2}(t^{\star}(x))^2} \tag{1}$$

$$c(x, \mu, \gamma) = \frac{1}{\pi\gamma[1 + (t^{\dagger}(x))^2]} \tag{2}$$

$$p(x, \eta, \mu, \sigma, \gamma) = \eta g(x, \mu, \sigma) + (1 - \eta)c(x, \mu, \gamma) \tag{3}$$

where $\eta \in [0, 1]$, $\sigma, \gamma, \in , R^{+}$, and $\mu \in R$ and

$$t^{*}(x) := \frac{x - \mu}{\sigma} \text{ and } t^{\dagger}(x) := \frac{x - \mu}{\gamma} \tag{4}$$

Concrete examples of symmetric profiles will be presented later in section III.E.3 . We now define the asymmetric profiles, where a is the asymmetry parameter: Eq. (5) defines the asymmetric Gaussian-like profile $\hat{g}$, Eq. (6) defines the asymmetric Cauchy-like profile $\hat{c}$, and Eq. (8) defines the asymmetric Pseudo-Voigt-like profile $\hat{p}$.

$$\hat{g}(x, \mu, \sigma, a) := \frac{1}{\sigma\sqrt{2\pi}} e^{-\frac{1}{2}\left(\frac{t^{*}(x)}{h(t^{*}(x), a)}\right)^2} \tag{5}$$

https://doi.org/10.1017/S0885715624000587 Published online by Cambridge University Press

$$\hat{c}(x,\ \mu,\ \ \gamma,\ a) := \frac{1}{\pi\gamma\left[1+\left(\frac{t^{\dagger}(x)}{h(t^{\dagger}(x),\ \ a)}\right)^{2}\right]} \tag{6}$$

where t^{*}, $t^{\dagger}$ are defined in Eq. (4) and

$$h(u,\ a) := 1 + \frac{au}{\sqrt{1+(1+a^{2})u^{2}}} \tag{7}$$

The function *h(u,a)* in Eq. (7), which uses the dimensionless asymmetry parameter a, is used to generate these asymmetric functions. It is crucial that the variable a remains dimensionless to ensure consistency and independence from the coordinate system. As a consequence, any variable like u introduced in subsequent equations, such as in Eq. (7), must also maintain this dimensionless property.

It is worth noting that when $a = 0$, the asymmetric profiles convert into the corresponding symmetric versions.

Finally, we define the asymmetric Pseudo-Voigt-like profile, wherein both the Gaussian-like and Cauchy-like profiles share the asymmetry parameter a:

$$\begin{aligned}\hat{p}(x,\ \eta,\ \mu,\ \sigma,\ \gamma,\ \ a)\ :& \\ &= \eta\hat{g}(x,\ \mu,\ \sigma,\ a) \\ &\quad + (1-\eta)\ \hat{c}(x,\ \mu,\ \ \gamma,\ \ a)\end{aligned} \tag{8}$$

where $\eta\ \in [0,\ 1]$, $\sigma,\ \gamma, \in R^{+}$, and $\mu,\ a \in R$. It is worth noting that the profiles from Eqs (5), (6), and (8) satisfy:

$$\hat{g}(\mu + x,\ \ \mu,\ \ \sigma,\ a) = \hat{g}(\mu - x,\ \ \mu,\ \ \sigma,\ -a) \tag{9}$$

$$\hat{c}(\mu + x,\ \ \mu,\ \ \gamma,\ a) = \hat{c}(\mu - x,\ \ \mu,\ \ \gamma,\ -a) \tag{10}$$

$$\hat{p}(\mu + x,\ \eta,\ \ \mu,\ \ \sigma,\ \ \gamma,\ a) = \hat{p}(\mu - x,\ \eta,\ \ \mu,\ \ \sigma,\ -a) \tag{11}$$

In other words, the profiles that are generated when changing a for $-a$ are reflections of each other from the vertical axis passing through the global maximum, which is allocated at $x = \mu$ (see Proposition 3). In subchapter "Illustration of Pseudo-Voigt profiles modified by asymmetry according to Eq. (8)", concrete examples of the asymmetric profiles can be seen.

B. Global maximum and magnitude of the showcased profiles

In Proposition 3, we prove that the proposed profiles defined by Eqs (5), (6), and (8) exhibit a distinctive property: they possess a unique critical point, which is an absolute maximum. Remarkably, the position and magnitude of this critical point remain invariant, irrespective of changes in the asymmetry parameter a. This property accelerates the convergence of the optimizer when fitting data with these profiles. In contrast, the general construction methods for asymmetric probabilistic distributions in the mathematical literature (e.g. Gupta et al., 2004; Huang and Chen, 2007) seem to lead to non-elementary profiles where the position and magnitude of the global maximum, strongly depend on the asymmetry parameter (We encountered difficulties in our attempts to construct an elementary asymmetric probabilistic distribution with the desired properties using these methods). The profiles in physics literature also exhibit these dependencies (see e.g., Kern, 1998; Korepanov and Sedlovets, 2018). This characteristic is not necessarily detrimental; if the dependencies accurately model the physical phenomenon under study, they can contribute positively to the fitting procedure.

It must be said that there are non-elementary profiles whose position and magnitude of the global maximum are independent of the asymmetry parameter e.g. (Kern, 1998). However, these non-elementary profiles add significant complexity when working with them in practice. The choice of asymmetric fitting functions for practical applications should be based on several criteria (see e.g., Korepanov and Sedlovets, 2018), such as a simple analytical form, the use of a minimum number of parameters, a description of the symmetric shape as a "zero case", the ability to estimate desired peak parameters in a straightforward way, and, most importantly, an adequate description of the experimental data.***Proposition 3.***

Let $\gamma,\ \sigma \epsilon R^{+}$, $\eta \epsilon [0,\ 1]$ and $\mu,\ a \epsilon R$ be arbitrary but fixed. Then, the profiles in Eqs (1)–(3),(5),(6) and (8) satisfy the following:

- $max(\hat{g}) = max(g) = \frac{1}{\sigma\sqrt{2\pi}}$;
- $C(\hat{g}) = M(\hat{g}) = M(g) = \{\mu\}$;
- $max(\hat{c}) = max(c\ ) = \frac{1}{\gamma\pi}$;
- $C(\hat{c}) = M(\hat{c}) = M(c) = \{\mu\}$;
- $max(\hat{p}) = max(p) = \eta\frac{1}{\sigma\sqrt{2\pi}} + (1-\eta)\frac{1}{\gamma\pi}$;
- $C(\hat{p}) = M(\hat{p}) = M(p) = \{\mu\}$.

The proof is an application of Proposition 2 over appropriately chosen functions.***Proof.***

We only prove statements two, four and six since the remaining statements follow immediately from these ones. Let us recall $h(x,\ a)$ from Eq. (7). It is easy to see that $h(x,\ a) > 0$ for any $x,\ a \epsilon R$, which implies that the function

$$r_{a}(x) := \frac{x}{h(x,\ a)}$$

is well defined over all

R for every $a \epsilon R$. Furthermore, it is clear that $r_{\ a}$ is a differentiable function over all R and with elementary calculations it is easy to verify that $r_{a}^{-1}(\{0\}) = \{0\}$, thus if $r_{a}(x) = 0$ then $x = 0$. In addition to this, elementary calculations show that $r_{a}' > 0$ for every $a \in R$, which in particular implies that $C(r_{\ a})$ is empty, i.e. it does not have critical points for every $a \in R$.

Let us introduce the following auxiliary functions:

$$g_{0} = \frac{1}{\sigma\sqrt{2\pi}} \cdot e^{-\frac{1}{2}x^{2}};$$

$$c_{0} = \frac{1}{\gamma\pi(1+x^{2})},$$

where $\mu,\ \gamma \in R^{+}$. These functions are clearly differentiable and it is easy to see that $M(g_{0}) = C(g_{0}) = \{0\}$, i.e. $g_{\ 0}$ has a unique critical point and this point is its absolute maximum, and likewise $M(c_{0}) = C(c_{0}) = \{0\}$. It follows directly from Proposition 2 that the functions $g_{0} \circ r_{a}$ and $c_{0} \circ r_{a}$ have a unique critical point located at $x = 0$ and this point is an

https://doi.org/10.1017/S0885715624000587 Published online by Cambridge University Press

absolute maximum. We also observe that

$$\hat{g} = (g_0 \circ r_a) \circ t^{\star};$$

$$\hat{c} = (c_0 \circ r_a) \circ t^{\dagger},$$

where $t^* = \frac{x-\mu}{\sigma}$ and $t^{\dagger}(x) = \frac{x-\mu}{\gamma}$. These equations and some elementary calculations show that $\hat{g}$ and $\hat{c}$ have a unique critical point at $x = \mu$ and this point is an absolute maximum. This proves statements two and four in the proposition.

To prove the last statement of the proposition, we first see that $\hat{p}$ has an absolute maximum and it is located at $x = \mu$. Indeed, let $x \in R\backslash\{\mu\}$, then

$$\hat{p}(x) = \eta \cdot \hat{g}(x) + (1-\eta) \cdot \hat{c}(x) < \eta \cdot \hat{g}(\mu) + (1-\eta) \cdot \hat{c}(\mu) = \hat{p}(\mu).$$

Thus, μ is the absolute maximum of $\hat{p}$. Now, we check that μ is the only critical point of $\hat{p}$. Elementary calculations show that the signs of $\hat{g}'(x)$ and $\hat{c}'(x)$ coincide. This means that the only way to satisfy the equation

$$\hat{p}'(x) = \eta \cdot \hat{g}'(x) + (1-\eta) \cdot \hat{c}'(x) = 0$$

where $0 \leq \eta \leq 1$ is when $\hat{g}'(x) = \hat{c}'(x) = 0$. And this happens if and only if $x = \mu$. Therefore $x = \mu$ is the only critical point of $\hat{p}$ and with this, the proof of the proposition is complete. ■

C. Area of the showcased profiles

In general, the areas of the asymmetric profiles in Eqs (5), (6), and (8) depend on the asymmetry parameter a and the mixing parameter η (as shown in Figure 1) ; therefore, these profiles are not probabilistic distributions (https://github.com/schnirelmann/AsymmetricProfilesFunctions). The area of these profiles can, however, be calculated efficiently and with good precision via numeric integration due to the elementary nature of the profiles. The area of the Cauchy-like profile [Eq. (6)] can even be calculated exactly using elementary complex analysis. In Figure 1, the area variation of the Pseudo-Voigt profiles with respect to the asymmetry parameter a is shown for $\eta = 0.0$, $\eta = 0.5$, and $\eta = 1.0$: more specifically, the y-axis shows the area of the asymmetric profile divided by the area of the symmetric profile and the x-axis shows the asymmetry parameter a.

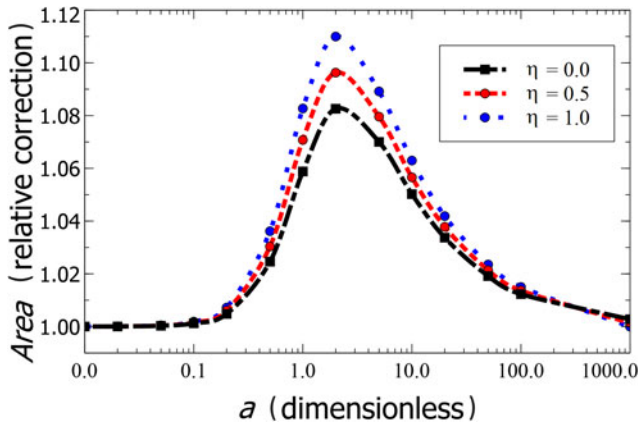


Figure 1. The y-axis shows the area of the asymmetric Pseudo-Voigt-like profile divided by the area of the symmetric Pseudo-Voigt profile, with the asymmetry parameter a varying along the x-axis. The different curves represent $\eta = 0.0$ (Cauchy-like), $\eta = 0.5$, and $\eta = 1.0$ (Gaussian-like).

Actually, the showcased profiles can be turned into probabilistic distributions by simply dividing the equations by the area of the profile, since their areas are finite. This would however make the peak's magnitude depend on the asymmetry parameter a but the highest point's position would remain intact. Nonetheless, the exact calculation of these areas is in some cases non-elementary and in many cases, it is not even clear if they can be calculated in closed form.

The general construction methods for asymmetric probabilistic distributions in the mathematical literature (e.g., Gupta et al., 2004; Huang and Chen, 2007) , deliver profiles with fixed area (and equal to one). However, these methods seem to lead to distributions where the position and magnitude of the global maximum, strongly depend on the asymmetry parameter, which is not suitable for the applications we are pursuing.

D. FWHM of the showcased profiles

The FWHM (full width at half maximum) of the profiles in Eqs (5), (6) and (8) is dependent on the asymmetry parameter a and mixing parameter η (see Figure 2) but since we know the magnitude of the profiles and the half maximum's magnitude exactly (see Proposition 3), the FWHM can be retrieved efficiently and with high accuracy with a simple binary search (https://github.com/schnirelmann/AsymmetricProfilesFunctions).

It is also worth mentioning that the FWHM of the profiles in the mathematical and physics literature often depends on the asymmetry parameter and is in general not easy to get in closed form. This makes the precision of a binary search for the FWHM depend on the precision of the estimation of the peak's magnitude; meaning, if we have a bad estimate of the peaks' magnitude, we also get a bad estimation of the FWHM by using a binary search.

E. Convolutions of symmetric and asymmetric profiles

In this subsection, we analyze how to approximate the convolutions of different combinations of symmetric and asymmetric profiles. Let us start with the symmetric case:

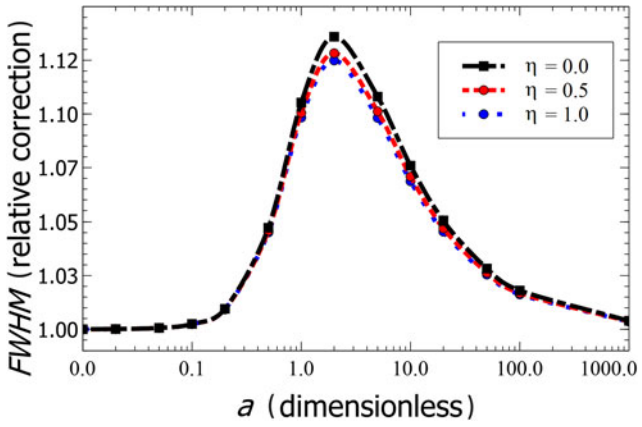


Figure 2. The y-axis shows the FWHM of the asymmetric Pseudo-Voigt-like profile divided by the FWHM of the symmetric Pseudo-Voigt profile, while the x-axis represents the asymmetry parameter a. The curves correspond to different values of η: $\eta = 0.0$ (Cauchy-like), $\eta = 0.5$, and $\eta = 1.0$ (Gaussian-like).

https://doi.org/10.1017/S0885715624000587 Published online by Cambridge University Press

1. Approximated convolution of symmetric profiles

The Gaussian and Cauchy functions, as well as their convolution, effectively describe symmetric profiles. Additionally, they possess certain properties that are useful for calculations, as discussed in detail by Balzar and Ledbetter (1994) . For example, the convolution of two Gaussian functions results in another Gaussian function with a combined variance given by with $\sigma^2_{result} = \sigma^2_1 + \sigma^2_2$, and the convolution of two Cauchy functions results in another Cauchy function with a combined width of $\gamma_{result} = \gamma_1 + \gamma_2$. The convolution of a Gaussian and a Cauchy function results in the Faddeeva function (Faddeeva and Terent'Ev, 1961), which can be approximated by a Pseudo-Voigt. This approach is less computationally intensive than a true convolution, yet provides an accuracy within 1% of the exact solution (Thomson et al., 1987) . We outline how the parameters of the Pseudo-Voigt approximating the Faddeeva function are calculated: given a Gaussian and Cauchy curves characterized by σ and γ, respectively, it's known that their peak widths can be characterized by the FWHM equations:

$$f_g = 2\sigma\sqrt{2ln(2)},\ f_c = 2\gamma. \tag{12}$$

In the next step, the parameters of the symmetric Pseudo-Voigt [see Eq. (3)] are calculated, which provide a good approximation of the convolution between the Gaussian and the Cauchy curves. The relevant equations for FWHM f and η_p and the methodology have been adopted from (Thomson et al., 1987):

$$f = \left(f_g^5 + 2.69269 f_g^4 f_c + 2.42843 f_g^3 f_c^2 + 4.47163 f_g^2 f_c^3 + 0.07842 f_g f_c^4 + f_c^5\right)^{1/5} \tag{13}$$

$$1 - \eta_p = 1.36603\left(\frac{f_c}{f}\right) - 0.477163\left(\frac{f_c}{f}\right)^2 + 0.11116\left(\frac{f_c}{f}\right)^3 \tag{14}$$

A specific example is presented in which a Gaussian curve with $\sigma = 1$, $\mu = 0$, corresponding to a FWHM of $f_g = 2.35482$, is convolved with a Cauchy function with $\gamma = 1$, $\mu = 0$, corresponding to a FWHM of $f_C = 2$. Using Eqs (13) and (14), the symmetric Pseudo-Voigt FWHM is calculated to be $f =$ 3.59225, and the Cauchy content is 1-$\eta_p = 0.631811$. The corresponding parameters of the Gauss and Cauchy components are: $\sigma_p = \frac{f}{2\sqrt{2\ln(2)}} = 1.52549$ and, respectively, $\gamma_p = \frac{f}{2} = 1.79613$. Figure 3 shows the Gaussian (with $\sigma = 1$) and Cauchy (with $\gamma = 1$) profiles and the result of their convolution, approximated with the procedure of Thomson et al. (1987).

2. Illustration of Pseudo-Voigt profiles modified by asymmetry according to Eq. (8)

In Figure 4, we present some examples of Pseudo-Voigt-like for $a = 0$ (symmetric case), $a = 0.5$, $a =$ 1.0, and $a = 2.0$. We set $\sigma_p = \frac{f}{2\sqrt{2ln(2)}} = 0.42466$ and $\gamma_p = \frac{f}{2} = 0.5$ so that f equals 1.0.

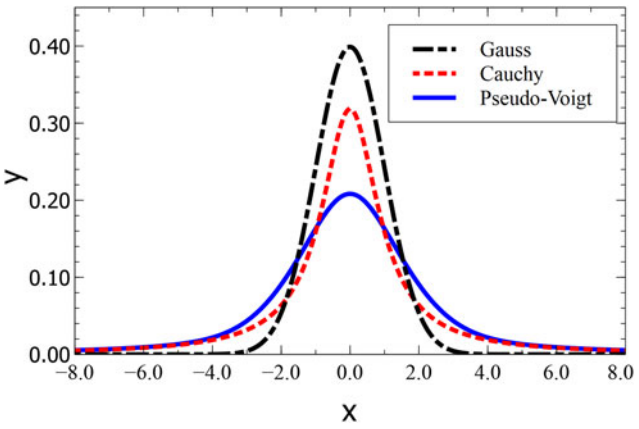


Figure 3. Examples of symmetrical distributions: Gaussian function with $\sigma = 1, \mu = 0$; Cauchy function with $\gamma = 1, \mu = 0$; Pseudo-Voigt function with $\sigma_p =$ 1.52549, $\gamma_p = 1.79613$, Cauchy part $1-\eta_p = 0.63181$, and $\mu = 0$, which approximates the convolution of the Gaussian and Cauchy functions.

3. Convolution of the showcased profiles with symmetric and asymmetric versions

In the measured diffractograms, a considerable part of the peak broadening can be attributed to the measurement system itself. The diffractogram can be represented as a convolution of a diffractometer-dependent part G and the sample-dependent part S. The diffractometer- dependent part G can now be represented as a convolution integral of the emission profile of the tube W and the slit system B (Cheary and Coelho, 1992).

$$Y(\theta) = G*S = B*W*S \tag{15}$$

The emission profile can be represented as a finite sum of symmetric Pseudo-Voigt profiles, with the Gaussian component typically neglected. The contribution caused by the slit system is asymmetrical (Cheary and Coelho, 1998). As shown in Wießner et al. (2005) , the device-dependent peak broadening can be determined by almost defect-free LaB_6. We can calculate this convolution with a reasonable precision 10^{-2} by simple numeric integration. Figure 5 shows the convolution between a symmetrical Pseudo-Voigt and an asymmetrical Pseudo-Voigt-like peak.

Figure 6 shows that the convoluted curve from Figure 5, along with three additional representative examples, can be accurately approximated (within a precision of 10^{-2}) by an asymmetric Pseudo-Voigt-like profile. For Figure 5, the following parameters were obtained: $\sigma = 0.87478$, $\gamma = 1.02997$ (resulting in $f = 2.05994$), Cauchy-like component $1-\eta = 1$, asymmetry parameter $a = 0.3676$, and a peak shift of $\Delta x =$ +0.2203. The four results are summarized in Table I . In practical applications, considering the peak shift is crucial when calculating the lattice plane spacing Δd from the peak position 2θ.

IV. APPLICATION OF AN ASYMMETRIC PROFILE FOR XRD ANALYSIS

A. Materials and method

In the suggested approximation, the measured diffraction peak is represented as a convolution of the instrumental and

https://doi.org/10.1017/S0885715624000587 Published online by Cambridge University Press

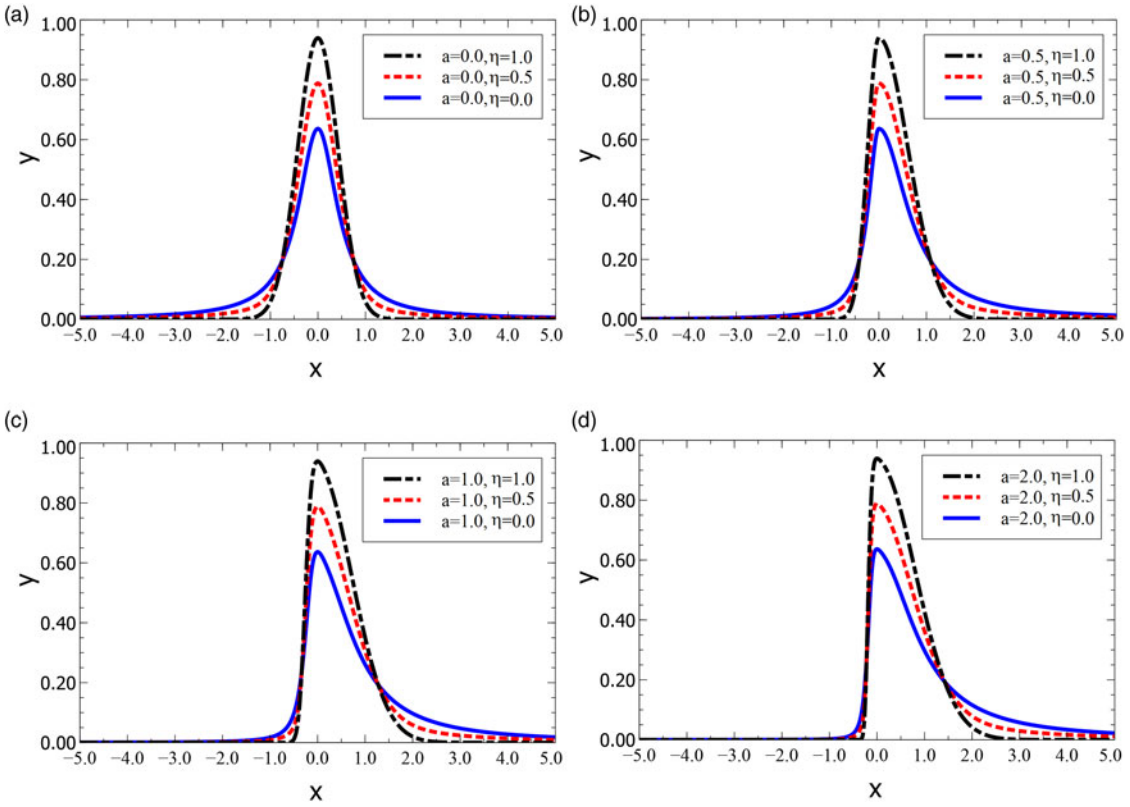


Figure 4. Asymmetric Pseudo-Voigt-like profiles with $\sigma_p = 0.42466$, $\gamma_p = 0.5$, $\mu = 0$ for different asymmetry parameters a, where for $a = 0.0$ the profile is the symmetric Pseudo-Voigt profile. The figure also shows profiles for different values of η: $\eta = 0.0$ (Cauchy-like), $\eta = 0.5$, and $\eta = 1.0$ (Gaussian-like).

sample broadening. XRD data were collected using a XRDynamic 500 from Anton Paar, Austria (Anton Paar, 2021). To accurately determine the instrumental broadening, which may include some degree of asymmetry, a nearly defect-free reference sample such as LaB_6 was used. This broadening is solely attributed to the diffractometer, allowing for the neglect of any broadening caused by deviations from an ideal lattice structure. The significance of this section lies in its relevance to s ection IV.C , where the method for isolating sample broadening from the overall profile will be detailed. Therefore, estimating the instrumental broadening is the primary focus of this section, with the instrumental broadening, as a function of 2θ, serving as input for further analysis.

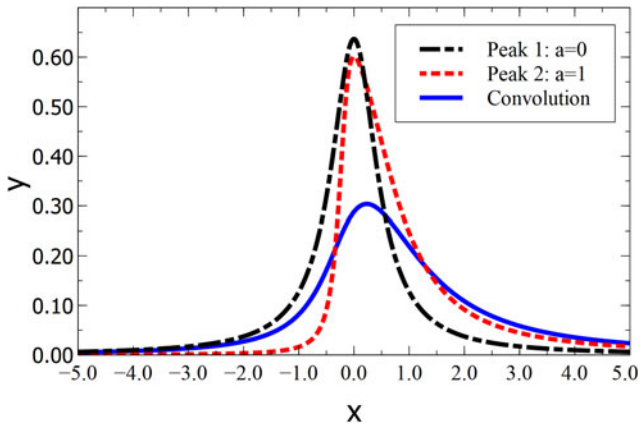


Figure 5. Convolution between symmetrical Pseudo-Voigt and asymmetrical Pseudo-Voigt-like peaks, each having an area equal to one. (Peak 1: $area_{p1} = 1.0$, $\sigma_{p1} = 0.425$, $\gamma_{p1} = 0.5$, i.e. $f_{p1} = 1.0$, Cauchy part $1-\eta_{p1} = 1.0$, $a_{p1} = 0.0$; Peak 2: $area_{p2} = 1.0$, $\sigma_{p2} = 0.425$, $\gamma_{p2} = 0.5$, i.e. $f_{p2} = 1.0$, Cauchy-like part $1-\eta_{p2} = 1.0$, $a_{p2} = 1.0$).

The XRD measurements were performed using a Bragg-Brentano geometry, equipped with a primary beam monochromator to suppress Kβ radiation and reduce background caused by Bremsstrahlung. The detector employed was a Pixos 2000 solid-state hybrid detector from Advacam, based on the Timepix3 chip architecture developed by CERN. It operated in 1D mode by summing signals from the 2D array. A step-scan procedure was used to accumulate the signals, resulting in the final diffractogram, as described by Cheary and Coelho (1994). The primary divergence slit was set to 0.25°, and no Soller slits were used.

The X-ray generator was configured to operate at 50 mA and 40 kV, with a goniometer radius of 400 mm. Scans were conducted over a 2θ range of 18.000° to 128.000° at a step size of 0.01° and a count time of 1.31 s per step. The experiment was carried out at ambient conditions (22 ± 1 °C) using Cu Kα radiation.

The sample used in this study was LaB_6 (NIST 660c), as specified by Black et al. (2020). The peak parameters of the LaB_6 standard were determined using XRDanalysis 1.2, software that we co-developed (Wiessner et al., 2023) . The following parameters were extracted: peak position (2θ), *FWHM* , left and right half-width at half maximum (*Left HWHM* and *Right HWHM*), the Cauchy-like part ($1-\eta$), and the asymmetry parameter (a).

The peak area takes into account the combined contributions of the Kα_1 and Kα_2 components. The peak height is measured at the position corresponding to the Kα_1 peak, and

https://doi.org/10.1017/S0885715624000587 Published online by Cambridge University Press

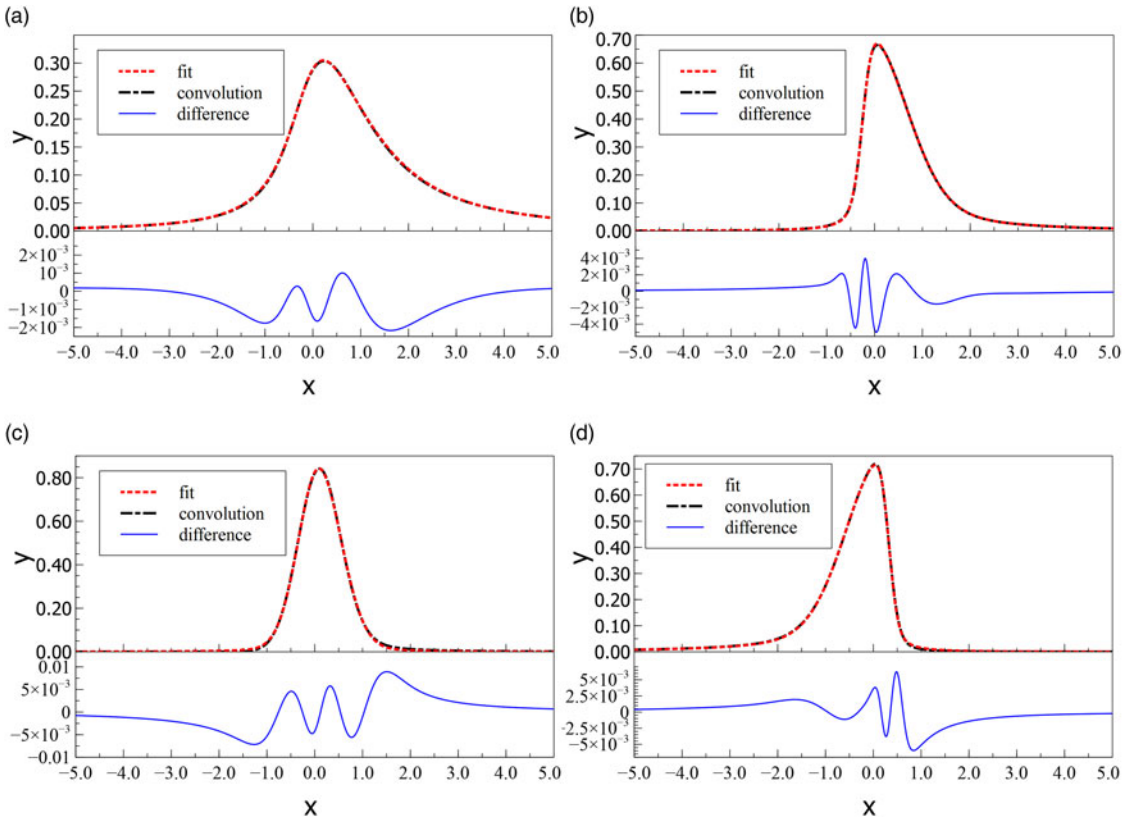


Figure 6. Asymmetric peak fits using asymmetric Pseudo-Voigt-like profiles (red) for the convoluted curves (black) from Figure 5 and three other representative examples. The difference between the fitted and convoluted peaks is shown in blue.

represents the sum of the intensities of both Kα_1 and Kα_2 components at this position. Further details are provided in the following section.

TABLE I. Optimized fitting parameters for approximating convoluted peaks using asymmetric Pseudo-Voigt-like profiles.

Description	FWHM	1–η (Cauchy-like component)	a	Shift: Δx
Variant 1:				
Peak 1	1	1	0	0
Peak 2	1	1	1	0
Approximated convolution	2.059	1	0.368	0.220
Variant 2:				
Peak 1	0.2	0.5	0	0
Peak 2	1	0.5	1	0
Approximated convolution	1.096	0.563	0.710	0.055
Variant 3:				
Peak 1	1	0	0	0
Peak 2	0.2	0.5	1	0
Approximated convolution	1.065	0.140	0.056	0.088
Variant 4:				
Peak 1	1	0.5	−1	0
Peak 2	0.2	0	1	0
Approximated convolution	1.047	0.496	−0.767	0.039

The table presents the parameters full width at half maximum (FWHM), Cauchy-like component (1−η), asymmetry parameter (a), and peak shift (Δx) for the convoluted curve from Figure 5 and three additional representative examples.

B. Peak profile analysis of Lanthanhexaboride (NIST 660c)

Instrumental broadening is caused by the limitations of the diffractometer itself, including the axial divergence. The axial divergence function is determined by the geometrical dimensions of the diffractometer system, such as the axial lengths of the X-ray source, sample, and receiving slit, as well as the angular apertures of the incident and diffracted Soller slits. More information can be found in Cheary and Coelho (1998) . If the divergence of the beam is high, it causes asymmetric instrumental broadening of the diffraction peaks. The work (Cheary and Coelho, 1998) describes how the diffractometer design and the extent of the axial divergence influence the shape of the axial divergence aberration function. However, it is important to note that reducing the divergence of the beam reduces the intensity of the diffraction pattern, so trade-offs may need to be made depending on the specific needs of the experiment.

In this section, we analyze the diffraction peaks of LaB_6 (NIST 660c) powder measured by the XRDynamic 500 diffractometer.

For the analyses, both symmetric and asymmetric Pseudo-Voigt functions are used. The Cauchy-like component (1–η) and the Gaussian-like component (η) are defined by the parameter η, which ranges between 0 and 1. In the case of asymmetry, no constraints are imposed on the asymmetry term a during the optimization.

In the first part, symmetrical Pseudo-Voigts are used to model the measurement. The background is represented by Chebyshev polynomials. The residuals, or differences between the model and the measured data, are also plotted. The plot of the residuals allows us to assess the quality of the fit between

https://doi.org/10.1017/S0885715624000587 Published online by Cambridge University Press

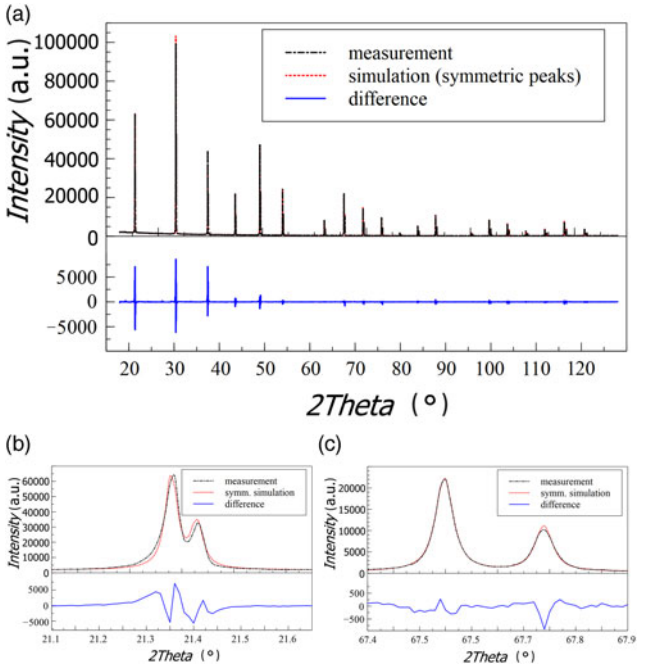


Figure 7. Measured LaB_6 powder (black curve (NIST 660c)) by a XRDynamic 500 from Anton Paar using a Cu Kα emission profile. The simulated diffractogram is represented by a symmetric peak fit model (red curve). The difference between the model and the measurement is in blue. In Figures 7(b) and 7(c) , we see two sections of Figure 7(a), where Figure 7(b) contains one diffraction peak with $hkl = (1\ 0\ 0)$ and Figure 7(c) contains one diffraction peak with $hkl = (2\ 2\ 1)$.

the measured data and the model. When the fit is good, the residuals are small and randomly distributed around zero, indicating that the model accurately describes the data.

1. Symmetric peak profile analysis of Lanthanhexaboride (NIST 660c) using Pseudo-Voigt Profiles

In this section, the measured diffraction pattern of LaB_6 is analyzed using symmetric Pseudo-Voigt profiles. Figure 7 illustrates the measurement, simulated diffraction patterns, and the residuals.

In the case of the symmetrical model, the fitting quality is poor, and the residuals are conspicuously large and systematically distributed. This indicates that the peak model inadequately represents the measured data. Particularly, for low 2θ values, such as $2\theta = 21.3°$ [see Figure 7(b)], the agreement is unacceptably low for many applications.

The parameters of the modeled symmetric Pseudo-Voigt peaks are summarized in Table II. One selected result from Table II is now also presented graphically. The broadening of the diffraction peaks, as a function of 2θ, is depicted in Figure 8. This graphical representation offers a clear visualization of the 2θ-dependent resolution of the diffractometer. It reflects the instrument broadening in this study, assuming that the peaks are symmetric, which is not the case.

2. Asymmetric peak profile analysis of Lanthanhexaboride (NIST 660c) using Pseudo-Voigt-like Profiles

To address the asymmetry in the diffraction peaks, we utilize the asymmetric peak fitting model (asymmetric Pseudo-Voigt-like profiles) described in Section III.A , which provides a more precise description of the peak shape. The result of the fitting procedure is presented in Figure 9.

As depicted in Figure 9, the application of an asymmetric Pseudo-Voigt-like profile model for XRD peak broadening, as shown, demonstrates strong agreement with the measured data. This is demonstrated by the small residuals and the visually good fit between the measured data and the model. The observed agreement between the model and data suggests that the asymmetric peak model is a reliable representation of this measurement. The parameters of the modeled peaks are summariz ed in Table III.

The broadening of the diffraction peaks, as a function of 2θ, is depicted in Figure 10. This representation allows a clear visualisation of the 2θ dependent resolution of the diffractometer for the used instrument settings in this study. The 2θ dependent behavior can be simulated using a polynomial fit, for example, a third-order polynomial

TABLE II. Table of symmetric diffraction peaks using symmetric Pseudo-Voigt profiles for LaB_6.

2θ (°)	FWHM (°)	η (rel.)	Height (cts.)	Area (cts.·°)
21.353	0.031	0.931	63 756	4365
30.381	0.033	0.792	102 827	7166
37.440	0.044	0.417	36 101	2869
43.506	0.033	0.855	21 675	1567
48.958	0.035	0.847	47 107	3594
53.990	0.038	0.819	24 022	1923
63.219	0.041	0.866	7927	701.1
67.548	0.041	0.908	22 075	2021
71.746	0.042	0.961	15 009	1422
75.844	0.043	0.971	9590	943.4
79.869	0.051	0.710	1502	155.0
83.845	0.053	0.831	5211	589.7
87.791	0.054	0.877	5212	1235
95.669	0.055	1.000	1712	216.8
99.639	0.059	0.991	8005	1099
103.658	0.062	1.000	6426	929.6
107.746	0.070	0.908	2576	399.7
111.931	0.071	0.988	3588	586.8
116.242	0.075	1.000	7447	1298
120.719	0.083	0.976	3491	661.9

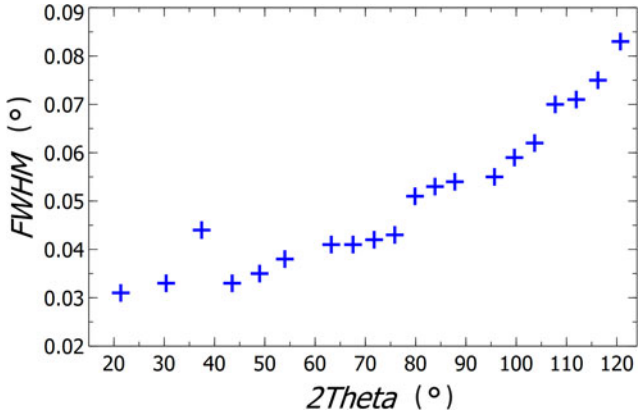


Figure 8. Full width at half maximum (*FWHM*) of the LaB_6 diffraction peaks using symmetric Pseudo-Voigt profiles (blue crosses).

https://doi.org/10.1017/S0885715624000587 Published online by Cambridge University Press

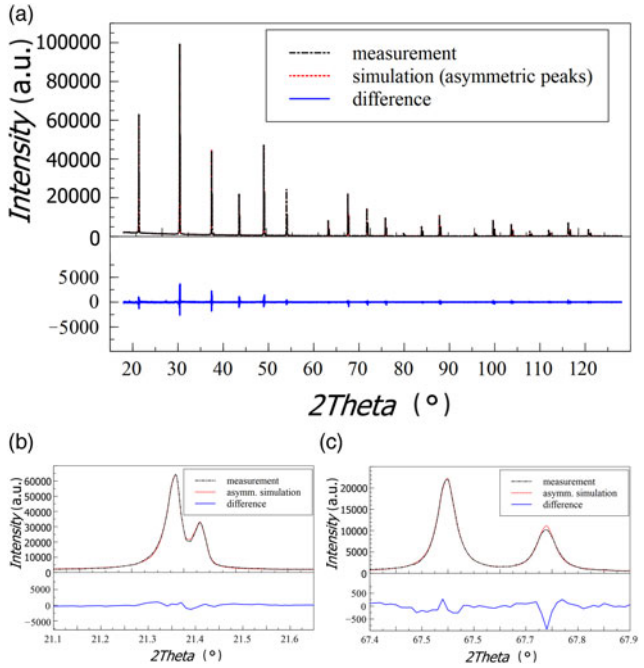


Figure 9. Measured LaB_6 powder (black curve (NIST 660c) by a XRDynamic 500 from Anton Paar using a Cu Kα emission profile. The simulated diffractogram is represented by an asymmetric Pseudo-Voigt-like fit model (red curve). The difference between model and measurement (residuals) is in blue. In Figures 9(b) and 9(c) , we see two sections of Figure 9(a), where Figure 9(b) contains one diffraction peak with hkl = (1 0 0) and Figure 9(c) contains one diffraction peak with hkl = (2 2 1).

(2θ in deg):

$$\mathrm{FWHM} = 4.9278 \cdot 10^{-8} \cdot (2\theta)^3 - 3.9390 \cdot 10^{-6} \cdot (2\theta)^2 + 2.2250 \cdot 10^{-4} \cdot 2\theta + 2.831 \cdot 10^{-2} \quad (16)$$

This polynomial fit is also presented in Figure 10.

The 2θ dependent asymmetry a of the diffraction peaks is shown in Figure 11 . This asymmetry is primarily caused by axial divergence. To model this effect, it can be approximated using a polynomial fit, specifically a fourth-order polynomial (with 2θ in degrees, Eq. 17):

$$a = -2.4523 \cdot 10^{-8} \cdot (2\theta)^4 + 8.0699 \cdot 10^{-6} \cdot (2\theta)^3 - 9.7554 \cdot 10^{-4} \cdot (2\theta)^2 + 5.2716 \cdot 10^{-2} \cdot 2\theta - 1.0673 + 5.2716 \cdot 10^{-2} \cdot 2\theta - 1.0673 \quad (17)$$

Additionally, the parameter 1–η, which indicates the proportion of the Cauchy component, is shown in Figure 12. The dominant component in Figure 12 is the Cauchy component. As described in section III.E.3 , the emission profile is modeled using a Cauchy profile. For the selected diffractometer settings (e.g., slit system), the resulting instrumental function, represented as a convolution, is dominated by the Cauchy part.

The error bars in Figure 12 are roughly approximated from the fluctuations in the data points. Additionally, the constraints that η lies between 0 and 1 are considered in the error bar estimation.

The simplest model to describe 1–η (Cauchy- like component) across the entire 2θ range is to use a constant value (mean value), 1–η = 0.938. This approach is justified because this parameter has only a minor influence during the convolution with peak broadening. Moreover, 1–η = 0.938 is within the error bars.

3. Comparison symmetric and asymmetric peak profile analysis of Lanthanhexaboride (NIST 660c) using Pseudo-Voigt and Pseudo-Voigt-like profiles

In addition to the model parameters, it is also useful to consider other goodness-of-fit measures as the residua, such as the R-values (Toby, 2006), in order to assess the overall quality of the fitted model. The values are presented and summarized in Table IV :

For simulation using asymmetry peaks, χ is found to be 1.64 for the asymmetrical analysis which substantially exceeds the theoretical limit of 1.0.

TABLE III. Table of asymmetric diffraction peaks using asymmetric Pseudo-Voigt-like profiles for LaB_6.

2θ (°)	a (rel.)	FWHM (°)	Left HWHM (°)	Right HWHM (°)	η (rel.)	Height (cts.)	Area (cts.·°)
21.356	−0.310	0.033	0.020	0.013	0.895	63 186	4388
30.384	−0.186	0.030	0.017	0.013	1.000	104 232	7103
37.441	−0.049	0.033	0.017	0.016	0.826	43 820	3108
43.507	−0.037	0.033	0.017	0.016	0.857	21 673	1551
48.958	−0.025	0.035	0.018	0.017	0.850	47 109	3551
53.990	−0.012	0.037	0.019	0.018	0.834	24 022	1915
63.219	0.003	0.040	0.020	0.020	0.861	7927	699.9
67.548	0.001	0.040	0.020	0.020	0.913	22 076	2020
71.745	0.010	0.042	0.021	0.021	0.963	15 010	1415
75.843	0.023	0.043	0.021	0.022	0.985	9589.9	938.7
79.867	0.089	0.049	0.023	0.026	0.814	1502	156.9
83.844	0.063	0.048	0.023	0.025	0.974	5418	593.6
87.790	0.025	0.050	0.024	0.026	0.997	10 783	1239
95.667	0.072	0.055	0.026	0.029	1.000	1712	215.6
99.639	0.030	0.059	0.029	0.030	1.000	8007	1093
103.656	0.063	0.064	0.031	0.034	1.000	6167	915.9
107.744	0.088	0.067	0.032	0.036	0.998	2569	398.5
111.929	0.085	0.074	0.035	0.039	0.990	3437	580.6
116.239	0.074	0.078	0.037	0.041	1.000	7077	1278
120.717	0.071	0.085	0.040	0.045	0.995	3364	656.0

https://doi.org/10.1017/S0885715624000587 Published online by Cambridge University Press

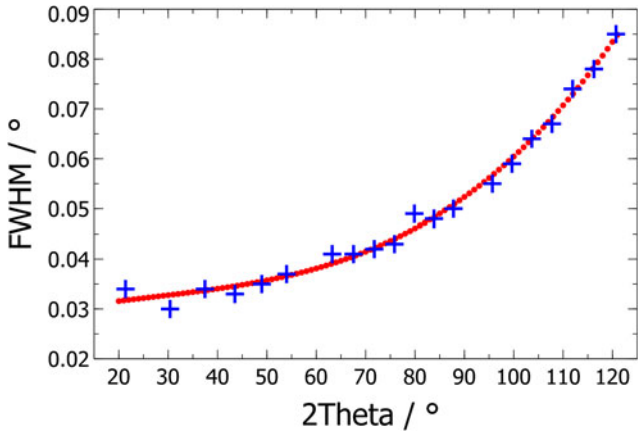


Figure 10. Full width at half maximum (*FWHM*) of the LaB_6 diffraction peaks, fitting using asymmetric Pseudo-Voigt-like profiles (blue crosses). The polynomial fit for *FWHM*, as described in Eq. (16) is represented by red points.

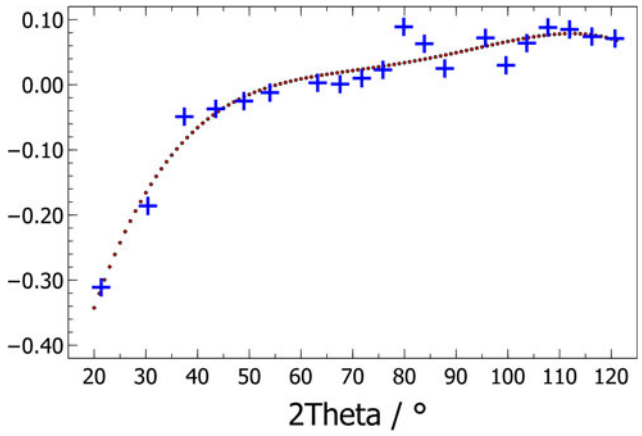


Figure 11. Asymmetric parameter a of the LaB_6 diffraction peaks using asymmetric Pseudo-Voigt-like profiles (blue crosses). The polynomial fit for a, as described in Eq. (17), is shown by red points.

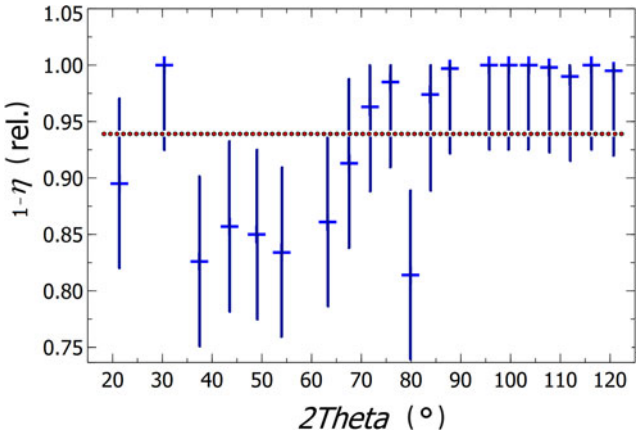


Figure 12. Cauchy component (1–η) and its associated error bars for the LaB_6 diffraction peaks, fitted using asymmetric Pseudo-Voigt-like profiles (with blue crosses representing the data points and lines indicating the estimated standard errors). The mean value for (1–η) is indicated by red points.

TABLE IV. *R*-values for symmetric and asymmetric peaks.

	Symmetric case	Asymmetric case
R_p (%)	5.44	4.24
R_{wp} (%)	7.51	5.60
R_{exp} (%)	3.41	3.41
χ (rel.)	2.20	1.64

C. Size-strain analysis of standard reference material "ZnO 60nm" from NIST 1979

In this chapter, asymmetric Pseudo-Voigt-like peaks are utilized for two specific examples. The first example uses these asymmetric peaks to determine peak positions and peak areas, which are then employed for qualitative phase analysis. In this case, the peak broadening effects caused by the diffractometer itself are not directly considered. The second example involves a size-strain analysis, where the peak broadening due to the diffractometer must be accounted for to obtain accurate values. The influence of the instrumental broadening is described in chapter IV.2.2 and considered for the size-strain analysis.

In the first example, the qualitative analysis is demonstrated in the following subchapter.

1. Qualitative analysis of "ZnO 60nm" from NIST 1979

For qualitative analysis, it is sufficient to use asymmetric Pseudo- Voigt-like profiles for direct fitting to the powder pattern of the sample under investigation. Peak areas and positions can be determined from these fits. However, it must be noted, as demonstrated in s ection III.E.3 (convolution of the showcased profiles with symmetric versions), that peak positions may undergo slight shifts. In section III.E.3 , it is shown that this effect can be of magnitude 20% of the FWHM of the asymmetric peak broadening of the diffractometer, for $a = 1$. This means that for a typical instrument broadening of $FWHM = 0.1°$ in 2θ and a strong asymmetry ($a = 1$), a peak shift of 0.02° can be expected. Typical matching algorithms that search for possible candidates in databases e.g., in the Powder Diffraction File from ICSD (Gates-Rector and Blanton, 2019) handle this well. One qualitative phase analysis result of "ZnO 60nm", generated with XRDanalysis 1.2, is depicted in Figure 13.

For the next example in the next section, however, determining the instrumental broadening is mandatory.

2. Size-strain analysis of "ZnO 60nm" from NIST 1979

This section demonstrates the process of performing a size-strain analysis on the reference material ZnO from NIST 1979, which has a nominal particle size of 60 nm. The results obtained from this analysis are then compared with those reported in the literature (Cline et al., 2020).

The diffractometer configuration used here is identical to that for the LaB_6 example in s ection IV.B . The LaB_6 (NIST 660c) sample used was practically defect-free, so the observed broadening is attributed solely to instrumental effects. It's important to note that peak broadening data – specifically, these asymmetric Pseudo-Voigt profiles – are only available at the 2θ positions corresponding to the diffraction peaks of LaB_6. Therefore, the interpolation method described in section

https://doi.org/10.1017/S0885715624000587 Published online by Cambridge University Press

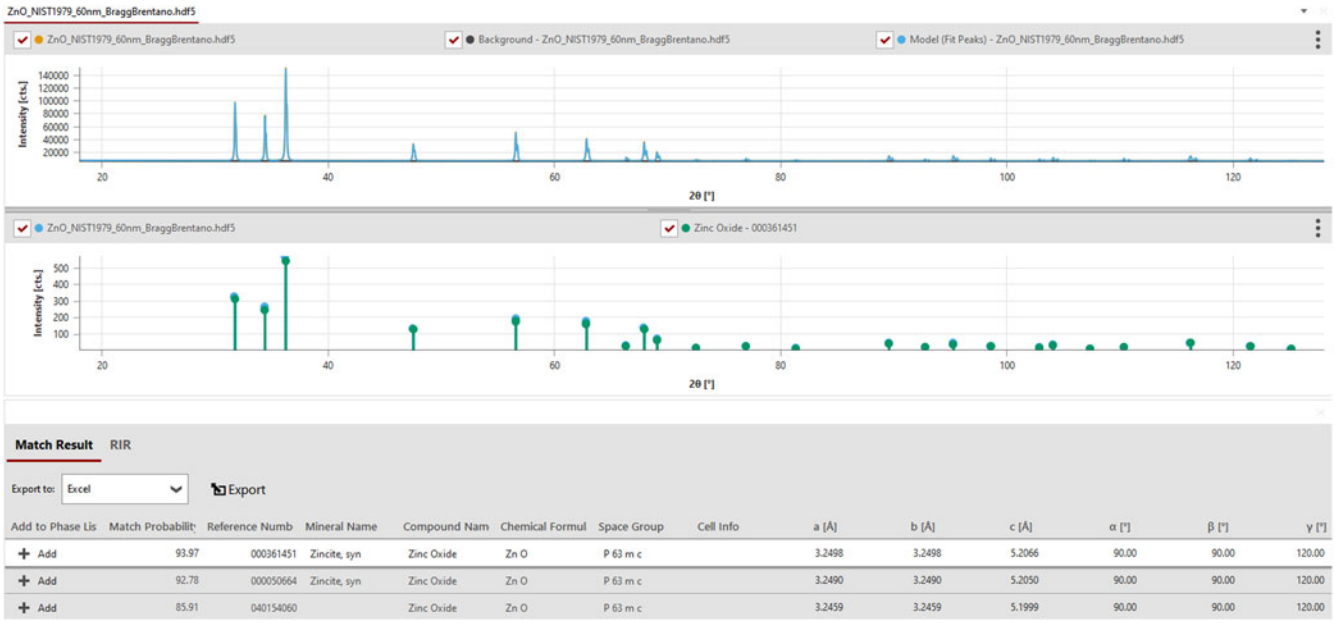


Figure 13. Result of the qualitative phase analysis by using XRDanalysis 1.2 (2023) with PDF-4 Axiom 2024 from ICSD (Gates-Rector and Blanton, 2019), for ZnO.

IV.B (polynomial fits) is used to estimate the relevant instrumental broadening across the entire measurement range.

Lattice strain and size effects induce peak broadening, which is described by symmetric Pseudo-Voigt functions. As previously described, the total broadening can be represented as a convolution of the instrumental broadening, modeled by asymmetric Pseudo-Voigt functions, with symmetric Pseudo-Voigt functions whose width depends on lattice strain and size effects. The following approach was used to determine the sample-dependent peak broadening:

The sum of squared errors is used as a metric to assess the deviation between the measured and simulated diffractogram. Using XRDanalysis 1.2, the background of the ZnO diffractogram was determined, described by Chebyshev polynomials, and subtracted from the measurement.

In the second step, initial values for the sample-dependent Pseudo-Voigt functions were determined. For this, FWHM, $1–\eta$ (Cauchy component), peak positions 2θ, and peak areas A were obtained using the peak search algorithm of XRDanalysis 1.2.

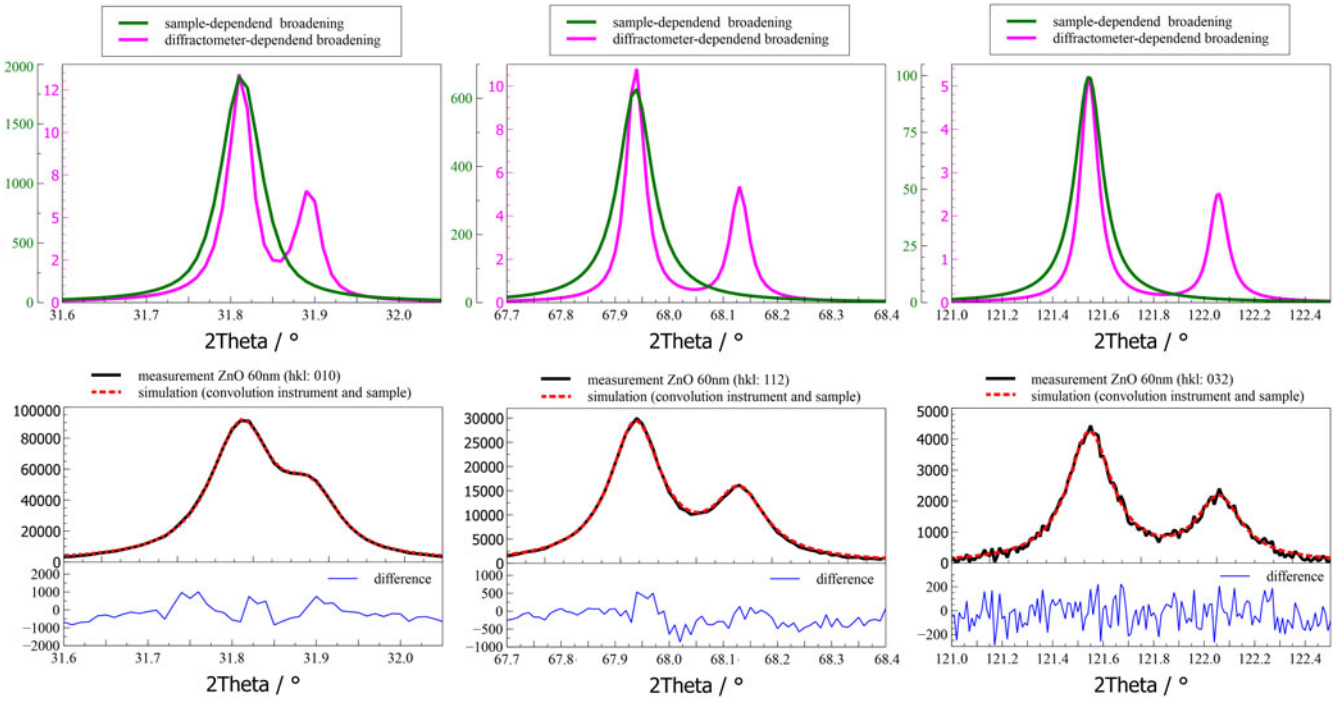


Figure 14. Optimized peak fitting results for ZnO at three different 2θ positions (31.763°, 67.938°, and 121.545°). The top section illustrates the two convoluted components contributing to the overall peak profile: the instrument-dependent asymmetric broadening ($K\alpha_1$ and $K\alpha_2$ components shown in magenta) and the sample-dependent broadening (green), illustrating the contributions from both the instrument and the sample to the overall peak profile.

https://doi.org/10.1017/S0885715624000587 Published online by Cambridge University Press

TABLE V. Peak analysis of NIST 1979 "ZnO 60nm" for the Williamson–Hall analysis.

2θ (°)	FWHM (°)	η (rel.)	IB (°)
31.763	0.0573	0.818	0.0828
34.415	0.0584	0.940	0.0892
36.247	0.0635	0.877	0.0942
47.532	0.0819	0.956	0.1260
56.588	0.0697	0.803	0.1001
62.848	0.0861	0.918	0.1301
66.366	0.0833	1.000	0.1308
67.938	0.0767	1.000	0.1205
69.075	0.0934	1.000	0.1467
72.552	0.0938	1.000	0.1473
76.948	0.0938	1.000	0.1473
81.374	0.1276	1.000	0.2004
89.597	0.1042	0.959	0.1605
92.777	0.1103	1.000	0.1733
95.290	0.1046	0.928	0.1589
98.598	0.1075	1.000	0.1689
102.916	0.1361	1.000	0.2138
104.113	0.1359	1.000	0.2135
107.416	0.1950	1.000	0.3063
110.368	0.1137	0.984	0.1772
116.254	0.1370	0.960	0.2112
121.544	0.1329	0.990	0.2078
125.126	0.1933	1.000	0.3036

In the third step, the symmetric Pseudo-Voigt parameters are optimi zed using the Optimization Toolbox from Matlab 2023b (The MathWorks Inc., 2023). The optimizer adjusts the symmetric Pseudo-Voigt parameters that are influenced by size and strain effects. The resulting Pseudo-Voigt functions are then convoluted with the instrument-dependent asymmetric Pseudo-Voigt-like function. As a result, the optimized sample-dependent Pseudo-Voigt parameters are obtained.

Some results after the optimization are shown in Figure 14 for three peaks at $2\theta = 31.763°$, 67.938°, and 121.545°. The figure is divided into three sections.

In the upper section, the two convoluted components are presented, specifically the instrument-dependent asymmetric broadening (consisting of two components – Kα_1 and Kα_2) and the sample-dependent contribution.

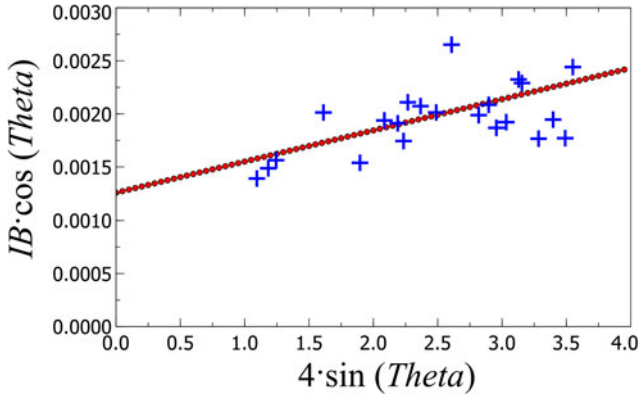


Figure 15. Williamson– Hall Plot using integral breadth *IB* instead of *FWHM* for NIST 1979 "ZnO 60nm". The determined intercept corresponds to $1.256 \cdot 10^{-3}$.

In the middle section, the measured peak and the simulated peak are displayed.

In the lower section, the residuals between the measurement and simulation are shown to assess the fit.

The middle section compares the measured diffraction peaks (black) with the simulated peaks (red) after optimization.

The bottom section displays the residuals (i.e., the differences between the measured and simulated peaks), providing an assessment of the fit quality.

To compare the results with the literature (Cline et al., 2020), the FWHM is converted into an integral breadth *IB*. In this transformation, the Pseudo-Voigt function corresponds to a rectangle with the same height and area as the Pseudo-Voigt function. The width of the rectangle aligns with *IB*. All determined values for the evaluation are presented in Table V . In the size-strain analysis conducted here, instead of the FWHM, *IB* is multiplied by $\cos(\theta)$ and compared with $4\sin(\theta)$ – see Figure 15.

Now, a linear fit, including error propagation (one sigma) using the formula from Wolberg (2006), is applied to the 23 data points in Figure 15 to determine the strain component from the slope and the size component from the *y*-intercept (e.g., Zak et al., 2011). Starting with the optimal linear fit, the sum of squared residuals is SSR $= 2.3558 \times 10^{-6}$.

The estimated variance *s* is calculated as:

$$s = \frac{2.3558 \times 10^{-6}}{23 - 1} = 1.12183 \times 10^{-7}$$

The *y*-intercept is 0.00126 ± 0.00025 and the estimated slope is 0.000294 ± 0.000095.

According to Cline et al. (2020), the volume-weighted domain size L_{vol} is calculated using the wavelength λ and the *intercept* from the Williamson– Hall plot, substituting the IB for FWHM:

$$L_{\mathrm{vol}} = \frac{\lambda}{intercept}$$

In this analysis, the volume-weighted L_{vol} is calculated as $L_{vol} = 0.154059\ \mathrm{nm}/1.26 \cdot 10\text{-}3 \approx (122 \pm 24)\ \mathrm{nm}$. The error is approximated by

$$122\,\mathrm{nm}\ \frac{0.00025}{0.00126} = 24\,\mathrm{nm}$$

This value is in good agreement with those reported by Cline et al. (2020), who found $L_{vol} = (138.9 \pm 0.6)$ nm using a high-resolution powder diffractometer at the 11-BM beamline at the Advanced Photon Source, and $L_{vol} = (128.3 \pm 25)$ nm using a Siemens D500 diffractometer equipped with a Johansson Ge 111 IBM, sample spinner, and scintillation detector with Cu Kα_1 radiation.

V. CONCLUSIONS

In this study, we developed a general method to construct asymmetric peaks. One of the main qualities of the construction method is that the magnitude and position of the global maximum of the constructed peaks are independent of the asymmetry parameter (see Propositions 2 and 3). With this

https://doi.org/10.1017/S0885715624000587 Published online by Cambridge University Press

method, we create an asymmetric Pseudo-Voigt-like profile [see Eq. (8)].

We fit real diffraction data measured on LaB_6 (NIST 660c) and ZnO 60 nm (NIST 1979) using an Anton Paar XRDynamic 500 diffractometer (Austria), with Cu Kα radiation.

The setup included a goniometer with a 400 mm radius, a Pixos 2000 solid-state hybrid detector, and a primary divergence slit set to 0.25°. See s ubsection IV .A for details on the diffractometer setup.

Additionally, we fit real data LaB_6 powder, see s ubsection IV.B with the classic symmetric Pseudo-Voigt profile [see Eq. (3)] and the asymmetric Pseudo-Voigt-like profile (see Figures 7 and 9). The quality of the fit was prominently better for the asymmetric function than for the symmetric function in the presented example. The Pseudo-Voigt-like profile is constructed with elementary functions, which facilitates the extraction of further mathematical properties of it (e.g. area, FWHM, convolutions) from which further physical information can be extracted. It must also be mentioned that the areas and FWHMs of the constructed profiles depend on the asymmetry parameter up to 10%, but they can be efficiently and accurately calculated using numeric methods.

In the end of this work, the asymmetric Pseudo-Voigt profile was still used in practical examples.

The asymmetric Pseudo-Voigt profile was commonly used in practical cases:

In s ection IV.B , the 2θ-dependent instrumental broadening was determined using a nearly defect-free NIST660c (LaB_6) standard.

In s ection IV.C.1 , NIST 1979 ("ZnO 60nm") was qualitatively analyz ed using the XRDanalysis 1.2 software package, in conjunction with the PDF database from the ICDD.

Peak positions and peak areas are determined using asymmetric pseudo-Voigt profiles. However, instrumental broadening was not considered in this case.

In s ection IV.C.2 , the instrumental broadening characteriz ed in s ection IV.B was analyzed using asymmetric Pseudo-Voigt profiles.

For the size-strain analysis, this was convoluted with symmetric Pseudo-Voigt profiles resulting from phase defects. Through inverse modeling, the 2Theta-dependent peak broadening was determined. A comparison with the volume-weighted domain size demonstrates good agreement with the findings of NIST.

In these three examples, it is demonstrated that the presented asymmetric Pseudo-Voigt profiles are practical and effective. Through their application, accurate characterizations of various materials and phenomena were achieved, showcasing their utility and reliability in real-world scenarios.

To provide an outlook: the Voigt profile, which is often approximated by a Pseudo-Voigt function, is widely employed to represent spectral line shapes in various fields of physics, including astrophysics, atmospheric spectroscopy, and plasma physics (Sampoorna et al., 2007). The method described can be applied in scenarios where peaks exhibit asymmetric behavior, and the function can be replaced by asymmetric Pseudo-Voigt-like functions, which are presented in this work.

ACKNOWLEDGEMENTS

The authors would like to extend their sincere gratitude to the anonymous reviewers for their invaluable ideas and remarks. Their constructive feedback greatly contributed to the improvement of this manuscript. Also, the author Abraham Gutierrez was kindly supported by project P-34763 of the Austrian Science Fund (FWF) during the preparation of this paper.

CONFLICT(S) OF INTEREST

This research did not receive any specific grant from funding agencies in the public, commercial, or not-for-profit sectors. The authors declare no conflict of interests.

REFERENCES

Alexander, L. 1954. "The Synthesis of X-Ray Spectrometer Line Profiles with Application to Crystallite Size Measurements." *Journal of Applied Physics* 25: 155–61.

Anton Paar. 2021. https://www.anton-paar.com/us-en/products/details/xrdynamic-500/ (download 20/10/2024).

Balzar, D., and H. Ledbetter . 1994. "Accurate Modelling of Size and Strain Broadening in the Rietveld Refinement: The 'Double-Voigt' Approach." *Advances in X-ray Analysis* 38: 397–404.

Black, D. R., M. H. Mendenhall, C. M. Brown, A. Henins, J. Filliben, and J. P. Cline . 2020. "Certification of Standard Reference Material 660c for Powder Diffraction." *Powder Diffraction* 35: 17–22.

Bragg, W. H., and W. L. Bragg . 1913. "The Reflection of X-Rays by Crystals." *Proceedings of the Royal Society of London. Series A, Containing Papers of a Mathematical and Physical Character* 88: 428–38.

Cheary, R. W., and A. Coelho . 1992. "A Fundamental Parameters Approach to X-Ray Line-Profile Fitting." *Journal of Applied Crystallography* 25: 109–21.

Cheary, R. W., and A. Coelho . 1994. "Synthesizing and Fitting Linear Position-Sensitive Detector Step-Scanned Line Profiles." *Journal of Applied Crystallography* 27: 673–81.

Cheary, R. W., and A. A. Coelho . 1998. "Axial Divergence in a Conventional X-Ray Powder Diffractometer. I. Theoretical Foundations." *Journal of Applied Crystallography* 31: 851–61.

Cheary, R. W., A. A. Coelho, and J. P. Cline . 2004. "Fundamental Parameters Line Profile Fitting in Laboratory Diffractometers." *Journal of Research of the National Institute of Standards and Technology* 109: 1–25.

Cline, J. P., M. H. Mendenhall, J. J. Ritter, D. Black, A. Henins, J. E. Bonevich, P. S. Whitfield, and J. J. Filliben . 2020. "The Certification of Standard Reference Material 1979: Powder Diffraction Line Profile Standard for Crystallite Size Analysis." *Journal of Research of the National Institute of Standards & Technology* 125: 1–39. doi:10.6028/jres.125.020.

Coelho, A. A. 2018. "TOPAS and TOPAS-Academic: An Optimization Program Integrating Computer Algebra and Crystallographic Objects Written in C++." *Journal of Applied Crystallography* 51: 210–18.

Davis, B. L. 1989. Quantitative Reference Intensity Analysis: Methodology and Means for Verification of Results in J. Hašek (Ed.), *X-Ray and Neutron Structure Analysis in Materials Science* (pp. 15–21). Boston, MA, Springer.

Davis, B. L. 1992. Quantitative Phase Analysis With Reference Intensity Ratio in E. Prince & J. K. Stalick (Eds.), *Accuracy in Powder Diffraction II: Proceedings of the International Conference May 26-29, 1992*(pp. 7–16).

Degen, T., M. Sadki, E. Bron, U. König, and G. Nénert . 2014. "The HighScore Suite." *Powder Diffraction* 29: 13–18.

Denney, J. J., G. S. Mattei, M. H. Mendenhall, J. P. Cline, P. G. Khalifah, and B. H. Toby . 2022. "Determination of Physically Based Pseudo-Voigt Powder Diffraction Profile Terms From the Fundamental Parameters Approach." *Journal of Applied Crystallography* 55: 289–95.

Faddeeva, V. N., and N. M. Terent'Ev . 1961. *Tables of Values of the Function W (z)*. Oxford/London/New York/Paris, Pergamon Press.

Gates-Rector, S., and T. Blanton . 2019. "The Powder Diffraction File: A Quality Materials Characterization Database." *Powder Diffraction* 34: 352–60.

Gupta, A. K., T. T. Nguyen, and J. A. T. Sanqui . 2004. "Characterization of the Skew-Normal Distribution." *Annals of the institute of statistical Mathematics* 56: 351–60.

https://doi.org/10.1017/S0885715624000587 Published online by Cambridge University Press

Huang, W.-J., and Y.-H. Chen . 2007. "Generalized Skew-Cauchy Distribution." *Statistics & Probability Letters* 77: 1137–47.

Hubbard, C. R., E. H. V. I. Evans, and D. M. Sedlovets. 1976. "The Reference Intensity Ratio, I/Ic, for computer Simulated Powder Patterns." *Journal of Applied Crystallography* 9: 169–74.

Kern, A. 1998. *Hochtemperatur-Rietveldanalysen: Möglichkeiten und Grenzen*. Heidelberg, Ruprecht-Karls-Univ.

Korepanov, V. I., and D. M. Sedlovets . 2018. "An Asymmetric Fitting Function for Condensed-Phase Raman Spectroscopy." *Analyst* 143: 2674–9.

Mittemeijer, E. J., and P. Scardi . (Eds.). 2013. *Diffraction Analysis of the Microstructure of Materials*. Berlin, Heidelberg, Springer Science & Business Media.

Rietveld, H. M. 1967. "Line Profiles of Neutron Powder-Diffraction Peaks for Structure Refinement." *Acta Crystallographica* 22: 151–2.

Rietveld, H. M. 1969. "A Profile Refinement Method for Nuclear and Magnetic Structures." *Journal of Applied Crystallography* 2: 65–71.

Sampoorna, M., K. N. Nagendra, and H. Frisch . 2007. "Generalized Voigt Functions and Their Derivatives." *Journal of Quantitative Spectroscopy and Radiative Transfer* 104: 71–85.

The MathWorks Inc . 2023. *MATLAB Version: 23.2.0.2380103 (R2023b)*. Natick, MA: The MathWorks Inc. https://www.mathworks.com.

Thomson, P., D. E. Cox, and J. B. Hastings . 1987. "Rietveld Refinement of Debye-Scherrer Synchrotron X-Ray Data From Al_2O_3." *Journal of Applied Crystallography* 20: 79–83.

Toby, B. H. 2006. "R Factors in Rietveld Analysis: How Good is Good Enough?" *Powder Diffraction* 21: 67–70.

Toby, B. H., and R. B. Von Dreele . 2013. "GSAS-II: The Genesis of a Modern Open-Source All Purpose Crystallography Software Package." *Journal of Applied Crystallography* 46: 544–9.

Wießner, M., S. Kleber, and A. Kulmburg . 2005. "In-Situ Investigation During Tempering of a High Speed Steel With X-Ray Diffraction." *Particle & Particle Systems Characterization* 22: 407–17.

Wiessner, M., M. Hipp, A. Gutierrez, and B. Bachofner . 2023. *XRDanalysis 1.2 (Computer Software)*. Graz, Anton Paar GmbH.

Wolberg, J. 2006. *Data Analysis Using the Method of Least Squares*. Berlin, Heidelberg, New York, Springer.

Zak, A. K., W. A. Majid, M. E. Abrishami, and R. Yousefi . 2011. "X-Ray Analysis of ZnO Nanoparticles by Williamson–Hall and Size–Strain Plot Methods." *Solid State Sciences* 13: 251–6.

https://doi.org/10.1017/S0885715624000587 Published online by Cambridge University Press